JOURNAL OF APPLIED PHYSICS **104**, 114306 (2008)

Secondary electron emission from freely supported nanowires

Makoto Suzuki,[1,a)] Kazuhiro Kumagai,[1] Takashi Sekiguchi,[1] Alan M. Cassell,[2] Tsutomu Saito,[3] and Cary Y. Yang[3]

[1]*Graduate School of Pure and Applied Sciences, University of Tsukuba, Ibaraki 305-8577, Japan and National Institute of Materials Science, Ibaraki 305-0044, Japan*
[2]*NASA Ames Research Center, Moffett Field, California 94035, USA*
[3]*Center for Nanostructures, Santa Clara University, Santa Clara, California 95053, USA*

(Received 6 September 2008; accepted 13 October 2008; published online 4 December 2008)

We present secondary electron (SE) emission results from freely supported carbon/silicon nitride (Si_3N_4) hybrid nanowires using scanning electron microscopy. We found that, contrary to bulk materials, the SE emission from insulating or electrically isolated metallic nanowires is strongly suppressed by the penetrating beam. A mechanism of the SE suppression by the positive specimen charging is proposed, which is based on a total emission yield calculation using the Monte Carlo technique. This finding provides an important basis for studying low-energy electron emission from nanostructures under a penetrating electron beam. © *2008 American Institute of Physics.*
[DOI: 10.1063/1.3032910]

I. INTRODUCTION

Since the discovery of the Malter effect[1] in 1936, secondary electron (SE) emission from insulators by electron bombardment has been a subject of experimental and theoretical studies for many decades, on a wide variety of applications including voltage contrast in scanning electron microscopy (SEM),[2–4] the field-enhanced SE emission,[5,6] microchannel plates,[7] plasma display panels,[8] and electron beam inspection tools[9,10] for electrical failure in ultralarge scale integration devices. Typical specimen configurations studied so far include a bulk insulator,[11,12] the thickness of which is much larger than the penetration depth of the primary electrons (PEs), and an insulating thin film formed on a bulk conductive substrate,[4,13] where the PEs may penetrate through the film thickness. Especially the latter configuration is of special importance because the relation between SE emission and surface charging forms the basis of SEM imaging and metrology for planar semiconductor devices with passivation layers.

Another important configuration, a thin insulator without any supporting substrate [freely supported insulator (FSI)] has not been investigated using SE emission. In fact, three-dimensional device structures which have been proposed for high-performance next-generation electronics require a FSI structure as a building block.[14–16] Thus in-depth understanding and proper interpretation of the SEM image of the freely supported nanomaterials including FSIs are strongly desired.[17] Here, we perform detailed analysis of the SEM contrast in one of the FSI structures, a freely supported nanowire. High-resolution scanning transmission electron microscopy (HR-STEM) and energy dispersive x-ray spectroscopy (EDS) confirm that the material under study is composed of a metallic carbon nanofiber (CNF) and an insulating silicon nitride (Si_3N_4) nanowire. The SEM images of the hybrid nanowire reveal that the SE emission from an insulating part as well as an electrically isolated metallic part of the nanowire is strongly suppressed by the penetrating beam. This phenomenon is explained using a proposed mechanism by which the positive charging of the specimen due to the penetrating electrons strongly reduces the low-energy electron emission.

II. EXPERIMENTAL

The nanowire used in this study was grown in the course of optimizing the vertically aligned CNF growth using plasma-enhanced chemical vapor deposition (PECVD) with nickel catalyst.[18] A 20-nm-thick nickel (Ni) catalyst layer was prepatterned on a silicon wafer to form catalyst density microarray chips,[18] which provide a high-throughput methodology to examine the CNF growth with varying catalyst island size (1–6 μm square) and catalyst spacing (10–20 μm) in a single chip (1.1×1.1 cm^2). A gas mixture of C_2H_2 and NH_3 (1:4) is kept at 4 Torr during the growth. Detailed reaction conditions are described elsewhere.[18,19] The present specimen is obtained from Ni islands less than 3 μm in diameter with 10 μm spacing. As-grown samples are carefully removed from the growth substrate to drop on the lacey Formvar/carbon network on the copper microgrid (200 mesh, Ted Pella) for imaging.

HR-STEM imaging is obtained using a Schottky-emission 200 keV STEM with a spatial resolution of 0.20 nm. EDS measurement is carried out with a standard Si(Li) x-ray detector mounted on a field-emission 30 keV SEM. For SEM imaging, another field-emission SEM (S-5500, Hitachi) is used, which enables one to vary beam energy from 0.5 to 30 keV with corresponding spatial resolutions of 1.6–0.4 nm. Probe current is also varied from 5 to 50 pA depending on the beam energy. The detectable energy windows for the signal electrons can be varied between the SE-dominated imaging (the energy of signal electrons $<20-50$ eV) and the backscattered-electron (BSE)–dominated imaging ($>20-50$ eV), by optimizing the Wien filter condition in the electron optics.[20]

[a)]Author to whom correspondence should be addressed. Electronic addresses: suzuki-makoto@naka.hiatchi-hitec.com.

 © 2008 American Institute of Physics

Author complimentary copy. Redistribution subject to AIP license or copyright, see http://jap.aip.org/jap/copyright.jsp

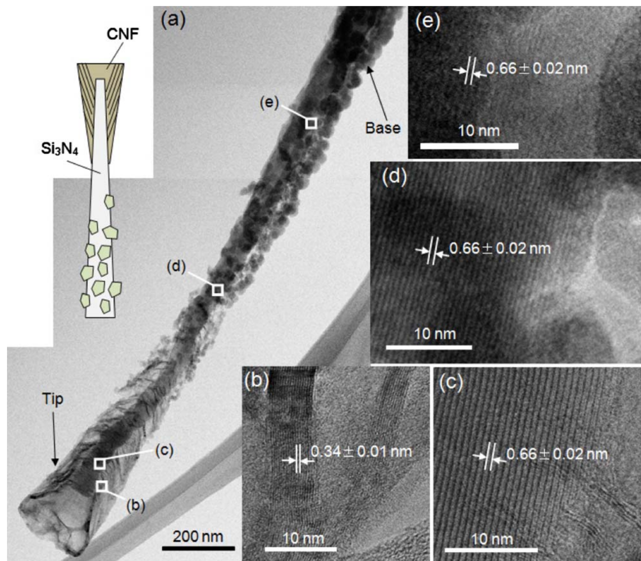

FIG. 1. (Color online) [(a)–(e)] HR-STEM images of carbon/silicon nitride hybrid nanowire. A stacked cone structure of graphitic layers with 0.34-nm spacing is observed at the tip, and the Si_3N_4 single crystal rod is also seen with 0.66-nm spacing. A schematic drawing of the nanowire structure is shown in the inset of (a).

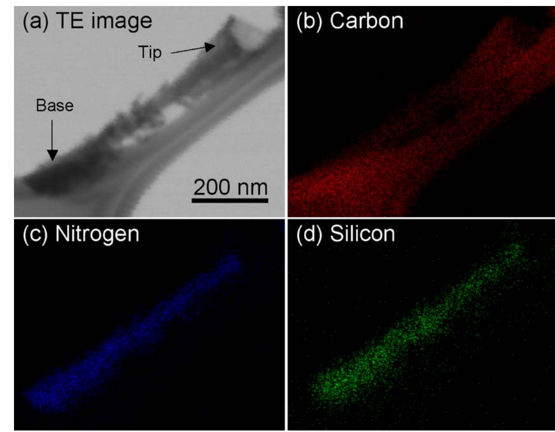

FIG. 2. (Color online) EDS mappings of the hybrid nanowire: (a) a TE image, (b) a carbon *K*-line map, (c) a nitrogen *K*-line map, and (d) a silicon *K*-line map.

III. RESULTS

A. Material characterization

Figure 1 shows HR-STEM images of typical as-grown nanowires. As shown in Fig. 1(a), the material has a one-dimensional structure with different morphologies at the tip and the base. The tip portion exhibits cup-shaped graphitic layers which is quite common in PECVD-grown CNFs.[21–23] The graphitic layers are confirmed by the observed hexagonal (002) lattice fringe with the spacing of 0.34 ± 0.01 nm as shown in Fig. 1(b). Under this CNF-like cap, a completely different single crystal rod with a lattice fringe spacing of 0.66 ± 0.02 nm is found [Fig. 1(c)]. This spacing is consistently found in the entire nanowire down to the base [Figs. 1(d) and 1(e)], forming a central rod of the nanowire. In other samples, different lattice fringes of 0.28 ± 0.01 and 0.43 ± 0.01 nm are also observed in similar parts of the nanowire. At the base of the sample, tiny particles are found, where no crystallinity is observed, suggesting that the particles are amorphous. Figure 2 shows the result of EDS elemental mapping of another nanowire with similar structure as in Fig. 1. Again the CNF structure is found at the tip as indicated in the STEM signal map [Fig. 2(a)], which is confirmed by the carbon *K*-line map in Fig. 2(b), where the signal is only observed at the tip area and at the Formvar network beside the sample as well. Nitrogen (*K*-line) and silicon (*K*-line) signals are mainly observed from the central rod, strongly suggesting the silicon nitride formation in the area. Indeed, all the lattice fringes observed in HR-STEM are consistent with those of the hexagonal α-Si_3N_4 single crystal as summarized in Table I. Here the lattice spacings of hexagonal α- and β-Si_3N_4 crystals are calculated by using the standard lattice constants of $a = 0.7588$ nm and $c = 0.5622$ nm and $a = 0.7604$ nm and $c = 0.2908$ nm, respectively.[24] Thus, we can conclude that the material is a hybrid nanowire composed of CNF and α-Si_3N_4, providing an ideal nanostructure for the study of SE emission from the FSI structure as schematically shown in the inset of Fig. 1(a). Unfortunately, the identification of the amorphous particles found at the base is difficult because of the absence of lattice fringes.

While the detailed discussion on the growth mechanism of the hybrid nanowires is outside the scope of the current work, it should be noted that during plasma-enhanced or microwave CVD deposition, an adequate supply of gas-phase nitrogen from the NH_3 feedstock gas and the solid silicon in the growth substrate can form Si_3N_4 nanostructures.[25–27] Thus, the catalytic growth of the silicon nitride portion of the wire could occur due to the local sputtering of the surrounding silicon substrate into the microenvironment where the Ni islands are patterned. The Ni particles then serve as catalyst to form the Si_3N_4 hybrid nanowire. It should be noted that we only observe the hybrid Si_3N_4/carbon nanowire formation when there is uncoated silicon substrate around the patterned Ni island, which ensures adequate supply of Si during the catalytic process occurring in the plasma-enhanced growth process.

B. Scanning electron microscopy of the hybrid nanowires

Figures 3(a)–3(d) show a series of SEM images of a hybrid nanowire on the lacey support with various beam energies ranging from 10 keV [Fig. 3(a)] down to 0.5 keV [Fig. 3(d)]. Image acquisition is performed with a single slow ras-

TABLE I. Comparison of the lattice fringe spacings (*d*) in HR-STEM with the actual lattice spacings for α- and β-Si_3N_4 with corresponding Miller indices (*hkl*).

	α-Si_3N_4		β-Si_3N_4	
Measured *d* (nm)	(*hkl*)	*d* (nm)	(*hkl*)	*d* (nm)
0.66 ± 0.02	(100)	0.672	(100)	0.657
0.28 ± 0.01	(002)	0.281	(101)	0.266
0.43 ± 0.01	(101)	0.431		

Author complimentary copy. Redistribution subject to AIP license or copyright, see http://jap.aip.org/jap/copyright.jsp

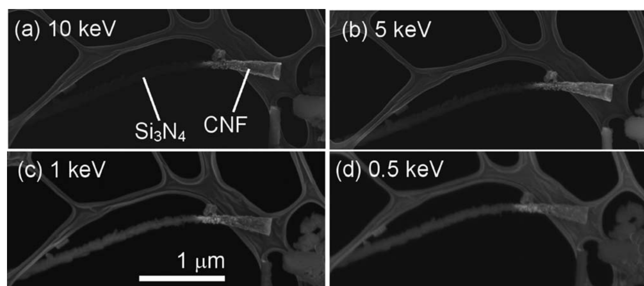

FIG. 3. Series of SE-dominated SEM images of carbon/silicon nitride hybrid nanowire with different beam energies of (a) 10, (b) 5, (c) 1, and (d) 0.5 keV. The CNF tip is in contact with the lacey support.

ter scan of the electron beam, which takes 20 s for each micrograph. The signal detector is used mainly to capture the SE signal. As can be seen in Fig. 3(a), the 10 keV image shows very weak SE signal intensity from Si_3N_4 compared with the CNF tip; thus the signal contrast between the CNF and Si_3N_4 is quite clear. This contrast, however, becomes less prominent at lower beam energies, and below 1 keV the SE signal from Si_3N_4 becomes comparable with that from the CNF. A characteristic length scale of the PE penetration depth called the maximum electron range R can be calculated using the Kanaya–Okayama formula[28] as

$$R = 27.6\frac{A}{\rho Z^{8/9}}E^{5/3}, \tag{1}$$

where R, A, ρ, Z, and E are the electron range in nanometers, the molecular weight in g/mol, the density in g/cm^3, the sum of the atomic numbers of consisting atoms, and the energy of PEs in keV, respectively. The material parameters of Si_3N_4 of $A=140.3$ g/mol, $\rho=3.44$ g/cm^3, and $Z=70$ lead to the result of $R=200$ nm at $E=3.5$ keV, which is the average diameter of the nanowire in Fig. 3. Therefore, it is reasonable to assume that the clear contrast between the CNF and Si_3N_4 portions is observed only when the PEs penetrate through the nanowire.

SE images of another nanowire with the similar morphology and diameter are shown in Fig. 4. Contrary to the case in Fig. 3, the image of the nanowire in Figs. 4(a)–4(d) shows no distinct contrast between the CNF and Si_3N_4 portions. At 30 keV the SE signal from both parts is much smaller than that from the support material [Fig. 4(a)], and gradually becomes comparable with decreasing beam energies [Figs. 4(b)–4(d)]. A notable difference between these two is whether the CNF tip of the nanowire is attached to support network (Fig. 3) or not (Fig. 4). This result implies that the electrical connection between the lacey support and the metallic CNF restores the SE emission even under the penetrating electron beam.

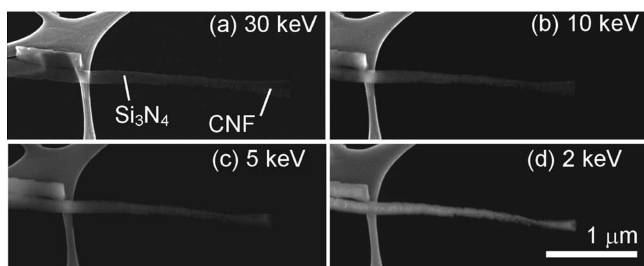

FIG. 4. Series of SE-dominated SEM images of carbon/silicon nitride hybrid nanowire with different beam energies: (a) 30, (b) 10, (c) 5, and (d) 2 keV. The CNF tip is electrically isolated.

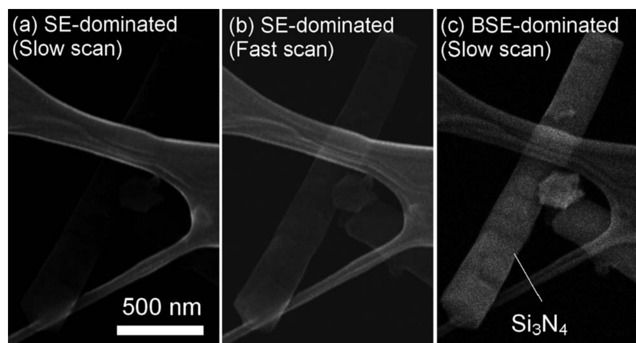

FIG. 5. The signal and scan-rate dependence of the SEM contrast of the Si_3N_4 nanowire with 30 keV beam: (a) SE-dominated image with a single slow scan (20 s), (b) SE-dominated image with multiple fast scans (40 ms/frame, 128-frame averaging), and (c) BSE-dominated image with single slow scan (20 s).

In Fig. 5, the differences in image contrast due to the scan rate and the signal type are shown. This nanowire has no CNF-like cap, forming a simple Si_3N_4 nanowire. The beam energy is fixed at 30 keV for all of these micrographs. Figures 5(a) and 5(b) show SE-dominated images, with a single slow raster scan (20 s) and multiple fast scans (40 ms/frame and 128-frame averaging), respectively. While in Fig. 5(a) the Si_3N_4 nanowire is almost invisible and only the lacey support can be seen, fast scans [Fig. 5(b)] make it slightly visible. Thus the SE signal intensity from the Si_3N_4 is scan-rate dependent, which is quite common in charge-related SEM contrast.[2] Another important signal comes from BSEs. Figure 5(c) shows the BSE-dominated image of the same nanowire. Contrary to the SE images [Figs. 5(a) and 5(b)], the Si_3N_4 rod emits a comparable amount of the BSE signal with the lacey support.

The experimental observations from the SEM images of the hybrid nanowires are summarized as follows:

(1) SE emission from Si_3N_4 is suppressed by the penetrating PEs [Figs. 3 and 5(a)].
(2) SE emission from CNF is suppressed by the penetrating PEs only when electrically isolated (Fig. 4).
(3) SE emission intensity is partially recovered by the fast and repetitive beam-scan [Fig. 5(b)].
(4) BSE emission is not suppressed by the penetrating PEs [Fig. 5(c)].

Due to the low-energy nature of SEs and the scan-rate-related signal intensity, specimen charging must be a key in understanding these results.

IV. DISCUSSION

A. Secondary electron emission from bulk insulator

In order to provide a satisfactory model to explain the experimental results, we first review the theory of SE emission from bulk insulator.[2,11] Generally in bulk samples, the number of total emitted electrons per PE, or the total emis-

Author complimentary copy. Redistribution subject to AIP license or copyright, see http://jap.aip.org/jap/copyright.jsp

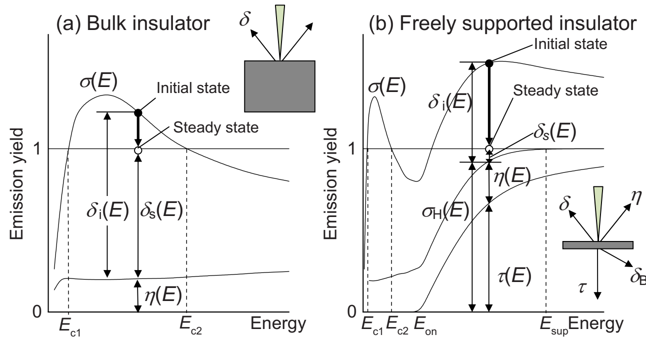

FIG. 6. (Color online) (a) Schematics of the electron emission yield $\sigma(E)$ of the bulk insulator. E_{c1} and E_{c2} are the crossover energies where $\sigma(E)$ becomes unity. $\eta(E)$ is the BSE yield, and $\delta_i(E)$ and $\delta_s(E)$ are the initial and steady-state values of the SE yield $\delta(E)$, respectively. Slight suppression of SE emission from the positively charged bulk specimen surface at steady state is illustrated. (b) Schematics of the electron emission yield of the FSI. E_{on} is the onset energy where the PEs start penetrating the sample. $\tau(E)$ and $\delta_B(E)$ are the TE yield and the SE yield from the back side, respectively. Strong suppression of SE emission from the positively charged freely supported film surface under the penetrating electron beam occurs above E_{sup}.

sion yield $\sigma(E)$, has a universal energy dependence[29] with a broad peak as shown in Fig. 6(a). There are two crossover energies E_{c1} and E_{c2} where the numbers of incoming and outgoing electrons are balanced; thus $\sigma(E_{c1})=\sigma(E_{c2})=1$. E_{c1} is typically less than 100 eV, and E_{c2} is between 500 eV and 2 keV, depending on the material. At $E_{c1}<E<E_{c2}$, $\sigma(E)$ is dominated by the SE yield $\delta(E)$, or the number of emitted SEs per PE, rather than the BSE yield $\eta(E)$, defined as the number of BSEs per PE, as shown in Fig. 6(a). Here we adopt a widely accepted convention that the SE is defined by the emitted electron whose kinetic energy is lower than 50 eV and the BSE energy is higher than 50 eV. In the case of insulating samples, $\sigma(E)>1$ $(E_{c1}<E<E_{c2})$ means positive charge accumulation in the specimen. The surface positive potential reduces the SE emission yield from the initial value $\delta_i(E)$ to the steady-state value $\delta_s(E)$; the electron balance is achieved,[7] i.e., $\sigma(E)=1$ [Fig. 6(a)]. Since the mean kinetic energy of SEs is about 2–5 eV, a weak positive charging up to a few eV is sufficient to stabilize the charging[7] [Fig. 6(a)]. At steady state, the SE emission yield is slightly reduced, but still remains dominant in $\sigma(E)$. When $\sigma(E)<1$ $(E<E_{c1}$ or $E>E_{c2})$ the negative potential is developed on the sample surface, resulting in the beam deceleration and the local field distortion.

B. Secondary electron emission from freely supported insulator

In FSI, the energy dependence of the total emission yield $\sigma(E)$ should be completely different from that of bulk insulator. Actually, in addition to the contributions from the BSE yield $\eta(E)$ and the SE yield $\delta(E)$, transmitted electron (TE) yield $\tau(E)$ and the SE emission yield from the back side $\delta_B(E)$ need to be added.[30] In order to calculate the total emission yield, a previously developed Monte Carlo simulation technique[31,32] is applied here. The PE trajectories are tracked down to 50 eV with a continuous energy-loss formula using the modified Bethe stopping power,[33,34]

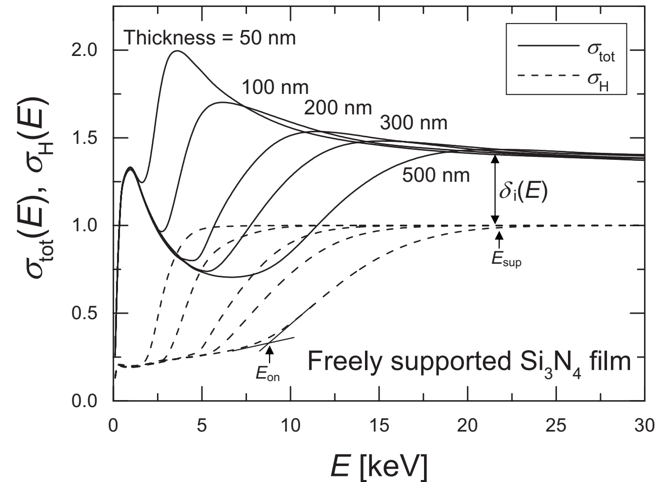

FIG. 7. Calculated total emission yield $\sigma(E)$ (solid curves) and high-energy electron emission yield $\sigma_H(E)$ (dotted curves) for five different Si_3N_4 film thicknesses of 50–500 nm using Monte Carlo simulation. Arrows indicate the two characteristic energies E_{on} and E_{sup} for 500-nm-thick Si_3N_4, which are defined as the onset energy of the electron transmission and the energy above which the sum of the TEs and BSEs is equal to the number of incident electrons, respectively.

$$-\frac{dE}{ds}=2\pi e^4\frac{N_A Z}{AE}\ln\left(\frac{1.166E}{J'}\right), \tag{2}$$

$$J'=\frac{J}{1+kJ/E}, \tag{3}$$

where s is the path length along the PE trajectory, e is the electron charge, N_A is the Avogadro number, k is a material constant, and J is the mean ionization energy of the material. A and Z are the molecular weight and the total atomic number, respectively. For Si_3N_4, $k=0.85$ and $J=115$ eV are used based on the Z dependence of these numbers.[34] The Mott elastic cross sections for silicon and nitrogen atoms provided in Ref. 35 are employed in the calculation. BSEs or TEs are counted when the PE scatters out of the specimen, depending on which side of specimen the electron escapes. Although the actual sample is cylindrical, an infinite sheet (thin film) is adopted for the simulation because it becomes straightforward to distinguish the BSEs and TEs in the film, and it does not alter the conclusion. Regarding SE emission, we assume that all energy loss ΔE by PEs along a finite step length Δs, $\Delta E=|dE/ds|\Delta s$, obtained from Eq. (2), is converted to the kinetic energy of generated SEs. Thus the number of generated SEs is obtained by dividing ΔE by the SE generation energy ε. This number inside the specimen at a particular depth exponentially decays with a mean free path λ before the SEs escaping from the specimen surface. λ and ε are fitted to reproduce the experimental E dependence of the SE yield.[29,31,32] For Si_3N_4, $\lambda=4.5$ nm and $\varepsilon=110$ eV were reported in Ref. 36.

The calculated total emission yields $\sigma(E)$ of the freely supported Si_3N_4 films with various thicknesses of 50, 100, 200, 300, and 500 nm are plotted in Fig. 7 with solid curves. As can be seen, after $\sigma(E)$ shows a small hump at around 1 keV, it increases again to form a broader peak. The small hump is due to the SE emission $\delta(E)$ from the entrance side

Author complimentary copy. Redistribution subject to AIP license or copyright, see http://jap.aip.org/jap/copyright.jsp

as in the bulk sample, and it is not affected by the film thickness because the major SE contribution is confined in the surface skin depth on the order of λ. The broader peak, however, strongly depends on the film thickness. To see the origin of this peak, we define the *high-kinetic-energy* emission yield $\sigma_H(E)$ as the sum of the BSE and TE yields $[\sigma_H(E)=\eta(E)+\tau(E)]$, which is plotted in the same figure with dotted curves. As shown in Fig. 7, it shows a steep increase at the onset of the broader peak of $\sigma(E)$. Since $\eta(E)$ has a weak energy dependence,[2] this increase comes mainly from the increase in $\tau(E)$ due to the penetration of PEs. The position of the peak is moved to higher energies with increasing thickness in accordance with Eq. (1).

By analogy with the bulk insulator case, the difference between $\sigma(E)$ and $\sigma_H(E)$ corresponds to the initial value of the total SE emission yield $\delta_i(E)$, and the difference between the horizontal line of $\sigma(E)=1$ and $\sigma_H(E)$ represents the steady-state value of the total SE emission yield $\delta_s(E)$ as shown in Fig. 6(b). Unlike the case of the bulk insulator, when the penetration depth $R(E)$ becomes much larger than the sample thickness t, $\sigma_H(E)$ approaches unity,

$$\sigma_H(E) = \eta(E) + \tau(E) \sim 1. \quad (4)$$

This means that all the incident PEs are backscattered or transmitted, not impeded inside the specimen. In this case, the initial value of the SE emission yield δ_i makes $\sigma(E)$ larger than 1, inducing positive charging. Since the steady-state solution imposes the condition

$$\sigma(E) = \sigma_H(E) + \delta_s(E) \to 1, \quad (5)$$

the comparison with Eqs. (4) and (5) leads to the complete suppression of the steady-state value of the SE yield, $\delta_s(E) \to 0$. This mechanism elucidates the suppression of the SE emission in Si_3N_4 under the penetrating PEs as well as electrically isolated CNF (observations 1 and 2). The CNF portion in contact with the support material does not show the SE suppression because the electron supply from the support material prevents it from charging. By reducing the beam energy, $\sigma_H(E)$ becomes much smaller than unity as in the bulk sample; thus the SE emission is not fully suppressed.

The SE signal increase by the fast scan can be explained in the following way. The discussion given here is based on the steady state of the specimen charging; thus the complete SE suppression is realized only when the positive charge accumulation is stabilized. A detailed theoretical study[4] of the charge irradiation on the SiO_2 film with comparable current density (10^{-5} A/cm^2) indicates that nearly 1 s elapses before a strong positive surface potential (~50 eV) is developed, which is far longer than the time interval between repetitive scans (40 ms). Thus the positive charging is not fully developed after each scan, leaving the SE signal finite under the fast scan (observation 3). Finally, the BSE signal intensity should not be affected much as long as the steady state is achieved by reducing the number of SEs having lower kinetic energies than BSEs (observation 4).

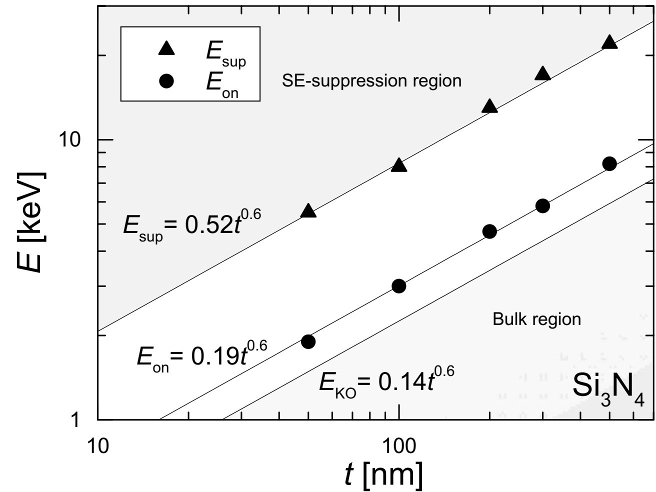

FIG. 8. Si_3N_4 thickness (t) dependence of the three characteristic energies, the onset energy E_{on}, the suppression energy E_{sup}, and the Kanaya–Okayama energy E_{KO}. E_{on} and E_{sup} are extracted from the Monte Carlo results in Fig. 7. E_{KO} is the minimum energy for penetration obtained from Eq. (1).

C. Thickness-energy relation for secondary electron suppression

Based on the result of the high-kinetic-energy emission yield $\sigma_H(E)$, two characteristic energies can be defined. One is the onset energy of the $\sigma_H(E)$ increase, E_{on}, where the PEs start penetrating, and the other is the suppression energy E_{sup}, above which the $\sigma_H(E)$ becomes unity and the suppression of SEs occurs. E_{on} is estimated by extrapolating the linear part of $\sigma_H(E)$ at the onset as schematically indicated in Fig. 7 for 500-nm-thick Si_3N_4. The estimation of E_{sup} is rather ambiguous since $\sigma_H(E)$ gradually converges to 1. Here we define E_{sup} as the energy at which the $\sigma_H(E)$ becomes unity with 1% tolerance; therefore $\sigma_H(E_{sup})=0.99$. Another characteristic energy can be defined as the Kanaya–Okayama energy E_{KO}, which corresponds to the minimum energy to penetrate the film. From Eq. (1), the relation between E_{KO} and the film thickness t is deduced as $E_{KO}=0.14t^{0.6}$ for Si_3N_4. E_{on} and E_{sup} extracted from Fig. 7 for each Si_3N_4 thickness are plotted in Fig. 8 as a function of the film thickness t together with E_{KO}. As expected, the onset energy E_{on} is close to but slightly larger than E_{KO}, and can be fitted with a similar curve $E_{on}=0.19t^{0.6}$. On the other hand, E_{sup} becomes much larger than E_{KO}, and is fitted by the formula $E_{sup}=0.54t^{0.6}$. This means that the beam energy required to suppress the SE emission is almost four times larger than the minimum energy of the beam transmission, E_{KO}. Upon the fitting, we assume that both energies have the same power of 0.6 as that of Kanaya–Okayama energy E_{KO}. Although a more precise fit with different formula would be possible, the errors in Monte Carlo simulation and in determining E_{on} and E_{sup} limit the accuracy of such fitting. The E-t region above the curve $E=E_{sup}(t)$ corresponds to the area where the SE emission is completely suppressed, and that below $E=E_{KO}(t)$ to the area where the specimen is considered as bulk in terms of beam irradiation, as indicated in Fig. 8.

V. CONCLUSION

A quantitative analysis of the SE emission from the freely supported nanowire has been presented. Strong sup-

Author complimentary copy. Redistribution subject to AIP license or copyright, see http://jap.aip.org/jap/copyright.jsp

pression of the SE signal in the insulating part, as well as in the electrically isolated metal, is well explained by the proposed model based on the positive charging induced by the penetrating beam. The relation between the specimen thickness and the beam energy for the SE signal suppression has been deduced using Monte Carlo simulation. The study provides an empirical model of SE emission from freely supported nanostructure, showing that the positive charging largely modifies the SEM image contrast of the nanoscale insulator, including thin films and nanowires.

ACKNOWLEDGMENTS

The authors are grateful to Yuko Isozaki of National Institute of Materials Science (NIMS) for her technical support in SEM imaging experiments and to Kevin Mcilwarth and Dr. Konrad Jarausch of Hitachi High-Technologies America, Inc., for their expert assistance with HR-STEM work. They are deeply indebted to Dr. Shigeo Tanuma, Dr. Hideki Yoshikawa, and Dr. Naoki Fukata of NIMS for fruitful and invaluable discussions.

[1] L. Malter, Phys. Rev. **50**, 48 (1936).
[2] L. Reimer, *Scanning Electron Microscopy*, 2nd ed. (Springer, Berlin, 1998).
[3] J. Cazaux, J. Appl. Phys. **59**, 1418 (1986); **85**, 1137 (1999).
[4] I. A. Glavatskikh, V. S. Kortov, and H.-J. Fitting, J. Appl. Phys. **89**, 440 (2001).
[5] H. Jacobs, Phys. Rev. **84**, 877 (1951).
[6] H. Jacobs, J. Freely, and F. A. Brand, Phys. Rev. **88**, 492 (1952).
[7] T. Jeong, J. Lee, S. G. Yu, S. Jin, J. Heo, W. Yi, D. Jeon, and J. M. Kim, J. Vac. Sci. Technol. B **19**, 866 (2001).
[8] G. Auday, Ph. Guillot, and J. Galy, J. Appl. Phys. **88**, 4871 (2000).
[9] H. C. Pfeiffer, G. O. Langner, W. Stickel, and R. A. Simpson, J. Vac. Sci. Technol. **19**, 1014 (1981).
[10] F. Mizuno, S. Mori, K. Satoh, K. Kanda, and H. Todokoro, J. Vac. Sci. Technol. **19**, 1019 (1981).
[11] X. Meyza, D. Goeuriot, C. Guerret-Piécourt, D. Tréheux, and H.-J. Fitting, J. Appl. Phys. **94**, 5384 (2003).
[12] J. P. Vigouroux, J. P. Duraud, A. Le Moel, C. Le Gressus, and D. L. Griscom, J. Appl. Phys. **57**, 5139 (1985).
[13] M. Miyoshi and K. Ura, J. Vac. Sci. Technol. B **23**, 2763 (2005).
[14] T. Rueckes, K. Kim, E. Joselevich, G. Y. Tseng, C.-L. Cheung, and C. M. Lieber, Science **289**, 94 (2000).
[15] H. E. Jeong, S. H. Lee, P. Kim, and K. Y. Suh, Nano Lett. **6**, 1508 (2006).
[16] C.-G. Huang, IEEE International Electron Devices Meeting 2006.
[17] M. Suzuki, Y. Ominami, Q. Ngo, C. Y. Yang, T. Yamada, A. M. Cassell, and J. Li, J. Appl. Phys. **100**, 104305 (2006).
[18] A. M. Cassell, Q. Ye, B. A. Cruden, J. Li, P. C. Sarrazin, H. T. Ng, J. Han, and M. Meyyappan, Nanotechnology **15**, 9 (2004).
[19] B. A. Cruden, A. M. Cassell, Q. Ye, and M. Meyyappan, J. Appl. Phys. **94**, 4070 (2003).
[20] S. Takeuchi, A. Muto, M. Nakagawa, S. White, R. Tamochi, M. Sato, M. Yamada, and D. C. Joy, Microsc. Microanal. **10**, (Suppl. 2) 950 (2004).
[21] M. Endo, Y. A. Kim, T. Hayashi, Y. Fukai, O. Oshida, M. Terrones, T. Yanagisawa, S. Hiragi, and M. S. Dresselhaus, Appl. Phys. Lett. **80**, 1267 (2002).
[22] H. Cui, X. Yang, M. L. Simpson, D. H. Lowndes, and M. Varela, Appl. Phys. Lett. **84**, 4077 (2004).
[23] Y. Ominami, Q. Ngo, A. J. Austin, H. Yoong, C. Y. Yang, A. M. Cassell, B. A. Cruden, J. Li, and M. Meyyappan, Appl. Phys. Lett. **87**, 233105 (2005).
[24] JCPDS File No. 41-360; JCPDS File No. 33-1160.
[25] Y. Chen, L. Guo, and D. T. Shaw, J. Cryst. Growth **210**, 527 (2000).
[26] Y. Fu, C. Q. Sun, H. Du, and B. Yan, Surf. Coat. Technol. **160**, 165 (2002).
[27] H. Y. Kim, J. Park, and H. Yang, Chem. Phys. Lett. **327**, 269 (2003).
[28] K. Kanaya and S. Okayama, J. Phys. D **5**, 43 (1972).
[29] K. Kanaya and H. Kawakatsu, J. Phys. D **5**, 1727 (1972).
[30] L. Reimer, U. Golla, R. Böngeler, M. Schindler, and R. Senkel, Optik (Stuttgart) **92**, 14 (1992).
[31] M. Suzuki, T. Yamada, and C. Y. Yang, Appl. Phys. Lett. **90**, 083111 (2007).
[32] M. Suzuki, Q. Ngo, H. Kitsuki, K. Gleason, Y. Ominami, C. Y. Yang, T. Yamada, A. M. Cassell, and J. Li, J. Vac. Sci. Technol. B **25**, 1615 (2007).
[33] H. Bethe, Ann. Phys. **397**, 325 (1930).
[34] D. C. Joy and S. Luo, Scanning **11**, 176 (1989).
[35] Z. Czyżewski, D. O. MacCalium, A. Roming, and D. C. Joy, J. Appl. Phys. **68**, 3066 (1990).
[36] D. C. Joy, *Monte Carlo Modeling for Electron Microscopy and Microanalysis* (Oxford University, New York, 1995).

Author complimentary copy. Redistribution subject to AIP license or copyright, see http://jap.aip.org/jap/copyright.jsp